Journal of ELECTRONIC MATERIALS, Vol. 49, No. 1, 2020
https://doi.org/10.1007/s11664-019-07759-6

Realization of Improved Visible Light-Mediated Photocatalytic Activity of Al_2O_3 Nanoparticles Through Cobalt Doping

S. ANBARASU,[1,2] S. ILANGOVAN,[1] K. USHARANI,[1] A. PRABHAVATHI,[2,3] M. SUGANYA,[2] M. KARTHIKA,[2,4] C. KAYATHIRI,[2] S. BALAMURUGAN,[2] and A.R. BALU[2,5]

1.—PG and Research Department of Physics, Thiru Vi Ka Govt. College, Thiruvarur, Tamilnadu, India. 2.—PG and Research Department of Physics, AVVM Sri Pushpam College, Poondi, Tamilnadu 613503, India. 3.—PG Department of Physics, STET College for Women, Mannarkudi, Tamilnadu, India. 4.—PG Department of Physics, Bon Secours College for Women, Thanjavur, Tamilnadu, India. 5.—e-mail: arbalu757@gmail.com

Improved photocatalytic activity through cobalt (Co) doping has been reported for Al_2O_3 nanoparticles in this paper. Undoped and Co-doped Al_2O_3 nanoparticles have been synthesized via a precipitation method. Pure and Al_2O_3 nanoparticles exhibit a monoclinic crystal structure. The optical bandgap decreases from 3.80 eV to 3.64 eV with Co doping. Due to the red shift in the bandgap, the recombination rate of photo-induced electrons and holes decreases in the doped catalysts which improved their efficiencies against the degradation of rhodamine dye. A remarkable degradation efficiency of 95.45% is evinced for the 4 wt.% Co-doped Al_2O_3 catalyst and this was well acknowledged from its decreased crystallite size, decreased bandgap and increased photosensitivity values. An increased degradation rate constant value of 0.96649 min^{-1} observed for the 4 wt.% Co-doped Al_2O_3 catalyst also confirms this. The results obtained indicate that the Co-doped Al_2O_3 nanoparticles are potential candidates as visible light catalysts with remarkable degradation efficiencies against toxic dyes. Also, the realization of ferromagnetism confirms the regenerable and reusable quality of the Co-doped Al_2O_3 catalysts.

Key words: Doping, red shift, catalyst, degradation, reusable

INTRODUCTION

Nanoscaled metal oxides have been widely used in recent years as catalysts in dye degradation due to their prominent physical and chemical properties. The most often used metal oxide photocatalysts are zinc oxide (ZnO),[1] tin oxide (SnO_2),[2] titanium dioxide (TiO_2),[3] magnesium oxide (MgO),[4] zirconium oxide (ZrO_2),[5] etc. Aluminum oxide (Al_2O_3) is a low-cost, wide bandgap material (~ 9 eV) which exhibits good thermal stability and large breakdown electric field which makes it suitable as a gate insulator layer in the field of resistive random access memory (RRAM).[6] Al_2O_3 exists in γ, η, χ, δ, θ and α crystal structures (phases) depending on temperatures ranging from 700°C to 1200°C.[7] Al_2O_3 due to its amphoteric nature, hydrolytic stability and potential ability to convert catalytic activity finds application as a heterogeneous catalysis support for petroleum refinement and adsorbents.[8] Due to large specific surface area and the presence of a large number of crystalline structural defects, Al_2O_3 is widely used in applications such as microporous catalysts and ultra-hard coatings, in electroluminescent flat-screen displays, as fillers for ceramic matrix composite materials and as an efficient adsorbent for the decolorization of dyes such as crystal violet, phenol and malachite green.[9–13] Al_2O_3 nanoparticles can improve the wear resistance of organic polymers by preparing an

---

(Received May 29, 2019; accepted October 22, 2019;

ultraviolet (UV) curable hard coating.[14] The nontoxic and hydrolytic stable nature makes Al_2O_3 suitable as photocatalyst for dye degradation, and due to its insulating behavior, it acts as an energy barrier, thereby reducing the recombination rate of photo-excited electron–hole pairs.[15] However, as a homogeneous catalyst, Al_2O_3 exhibits poor degradation efficiency, especially under visible light due to its widened bandgap. But, when used as a partner along with other semiconductors in photocatalytic applications, Al_2O_3 plays a significant role in improving the degradation efficiency, due to the presence of acid sites on the Al^{3+} surface which mediates O_2 photo-adsorption inducing photoactivation of O_2 easily.[16] The photocatalytic task of Al_2O_3 under visible light could be improved by reducing its bandgap which could be achieved by doping with noble metals. In our earlier work, improvement in the photocatalytic performance of Al_2O_3 was realized under visible light through Zn^{2+} doping.[17] Ferromagnetism is an essential characteristic of a regenerable and reusable catalyst. Hence, to induce magnetization and to improve the photocatalytic performance of Al_2O_3, cobalt (Co^{2+}) doping has been performed in this work.

Co^{2+} is a transition metal ion which has an ionic radius of 0.74 Å that is slightly greater than Al^{3+} (0.51 Å) ion and, hence, when substituted into the Al_2O_3 matrix, it creates more lattice defects, thereby altering its properties significantly. Co^{2+} exhibits spin–orbit interaction and, hence, it is supposed to modify the electron transport phenomenon of Al_2O_3 by inducing magnetic moments on substitution.[18] It has been reported that Co doping decorated the electron structure of ZnO and improved its visible light absorption ability.[19] Miao et al.[20] reported that Co doping not only improved the visible light absorption but altered the surface atomic state of ZnO which is much more suitable for photocatalytic reaction. Co in SnO_2 facilitates electron efficiently from its conduction band to an oxygen molecule in dye solution, thereby enhancing its photodegradation ability.[21]

The precipitation method has been adopted in this work to synthesize Co-doped Al_2O_3 nanoparticles. Co doping concentration is varied as 0 wt.%, 2 wt.%, 4 wt.% and 6 wt.% of the amount of aluminum chloride used to synthesize Al_2O_3 nanoparticles. Besides the structural, optical and electrical properties, photocatalytic and magnetic properties were investigated, and the impact of Co^{2+} ions on the properties of Al_2O_3 was analyzed. Synthesis and studies on the photocatalytic and magnetic properties of Co-doped Al_2O_3 nanoparticles has not been reported earlier, and this is the first report on the studies performed. The hindrance of using Al_2O_3 nanoparticles as an effective catalyst under visible light irradiation has been shattered with Co doping, and this has been justified in this work. The main highlights of this work are: (1) optical bandgap decreased with Co doping, (2) increased photosensitivity has been realized with increase in Co doping concentration, (3) photodegradation efficiency increased with Co doping and (4) Co-doped Al_2O_3 nanoparticles exhibit ferromagnetic behavior. The highlighted results are compared with other similar studies in their respective sections.

EXPERIMENTAL DETAILS

Pure Al_2O_3 nanoparticles were synthesized by precipitating after aging for 4 h the aqueous solution (150 mL) containing 0.1 M aluminum (III) chloride ($AlCl_3$) and 10 mL liquid ammonia. The liquid ammonia concentration is varied as 5 mL, 10 mL and 15 mL to identify the best optimized pH value to synthesize Al_2O_3 nanoparticles. The pH values of the 5 mL, 10 mL and 15 mL of added liquid ammonia solutions were found to be 6, 10 and 13, respectively. With the pH value of 10, the precursor solution seems to be more basic, and the precipitation yield was found to be better. The precipitates were crushed after washing and calcined at 200°C for 1 h to form Al_2O_3 nanoparticles. By adding $CoCl_2{\cdot}6H_2O$ equal to 2 wt.%, 4 wt.% and 6 wt.% of the weight of $AlCl_3$ to the above prepared precursor solution, Co-doped Al_2O_3 nanoparticles were obtained. x-ray diffraction (XRD), surface morphology, Fourier transform infrared (FTIR), ultra violet-visible-near infrared (UV–Vis NIR) and photoluminescence (PL) studies of the Co-doped Al_2O_3 nanoparticles were performed using an x-ray diffractometer (X'-pert PRO Analytical PW 340/60), a HITACHI S-3000H scanning electron microscope, a Tecnai-20 G2 transmission electron microscope, a Perkin Elmer RX-1 spectrophotometer, a LAMBDA-35 UV–Vis-NIR double-beam spectrophotometer and a Varian Cary Eclipse fluorescence spectrophotometer, respectively. $I-V$ curves were drawn from the values of current obtained in the 1–10-V range using a Keithly 65176 electrometer. The photodegradation ability of the Co-doped Al_2O_3 nanoparticles was tested against rhodamine B (RhB) dye under visible light. In the photocatalytic tests, 6 mg (optimized value) of 0 wt.%, 2 wt.%, 4 wt.% and 6 wt.% Co-doped Al_2O_3 catalysts was added to four sets of 100-mL aqueous dye solutions containing 0.025 M RhB dye. To ascertain the concentration of Co in the tested catalysts, energy-dispersive x-ray (EDX) spectra was taken, and the amount of Co was found to be equal to 1.26 wt.%, 2.49 wt.% and 4.87 wt.% for the Al_2O_3 nanoparticles synthesized with 2 wt.%, 4 wt.% and 6 wt.% Co doping concentrations, respectively. One set of dye solution without any catalyst is used as blank reference to standardize the initial absorbance of RhB. The dye solutions with the catalysts were stirred under dark condition for 30 min to achieve adsorption–desorption equilibrium. Absorption spectra of RhB were recorded at $\lambda = 554$ nm to monitor the degradation process. Magnetization

(M)–magnetic field (H) curves were recorded using a Lakeshore 7410 vibrating sample magnetometer.

RESULTS AND DISCUSSION

Physicochemical Properties

Figure 1 shows the XRD patterns of the undoped (0 wt.% Co) and 2 wt.%, 4 wt.% and 6 wt.% Co-doped Al_2O_3 nanoparticles. XRD profiles indicate that the Co-doped Al_2O_3 nanoparticles crystallize with a monoclinic structure of θ-Al_2O_3 as the positions of the peaks matched with Joint Committee on Powder Diffraction Standards (JCPDS) card no. 86-1410. No Co-related peaks were observed even for the highest doping concentration, indicating the presence of an undetected level of contamination in the prepared Al_2O_3 samples. As seen in Fig. 1, with up to a 4 wt.% Co doping concentration, the presence of (1 1 0), (0 0 2), (2 0 2), (3 1 1), (1 1 2), (6 0 1) and (5 1 1) planes exactly matched with the undoped sample; however, for the 6 wt.% Co-doped sample, the (1 1 0) and (3 1 1) peaks seem to disappear, and this indirectly represents that up to a 4 wt.% doping concentration of Co^{2+} ions might have completely substituted Al^{3+} ions in the host matrix, and at 6 wt.% Co doping concentration, Co^{2+} ions might have occupied the interstitial sites, thereby deteriorating the lattice structure of Al_2O_3. In spite of this, all the samples had a strong (0 0 2) preferential growth, and the position of this peak seems to be slightly shifted towards a lower 2θ angle up to 4 wt.% Co doping concentration. For the 6 wt.% Co doping concentration, it seems to shift towards a higher angle. This shifting can be attributed to the change in the interplanar distance caused by the strain in the Al_2O_3 lattice generated by the incorporation of Co^{2+} ions.[22]

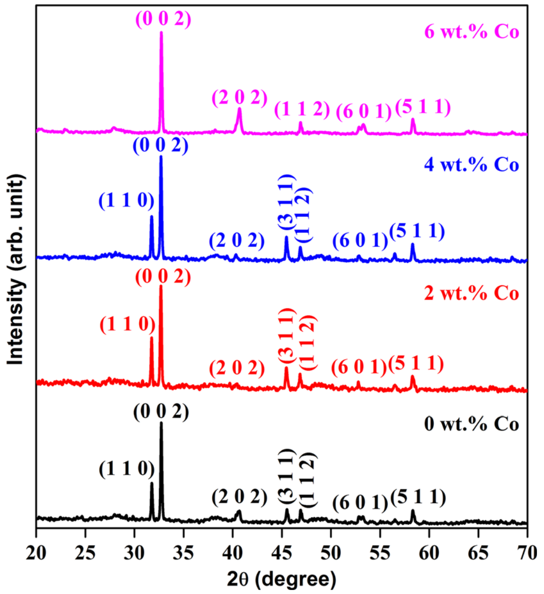

Fig. 1. XRD patterns of the 0 wt.%, 2 wt.%, 4 wt.% and 6 wt.% Co-doped Al_2O_3 nanoparticles.

The crystallite size (D) values given in Table I are estimated from the (0 0 2) diffraction plane of the Co-doped Al_2O_3 samples, using the Scherrer formula[23]:

$$D = \frac{0.9\lambda}{\beta \cos\theta} \tag{1}$$

where β is the full width at half maximum (FWHM), $\lambda = 1.5406\ \mathring{A}$ (wavelength of the x-ray source) and θ is the Bragg angle. Due to the substitution of Co^{2+} ions, grain boundary restraining takes place due to symmetry-breaking effects at the boundary limits of grain growth, and, hence, decreased crystallite sizes were obtained for the doped samples. Another possible reason for the decreased crystallite size realized with Co doping might be due to the Zener pinning effect.[24] The Zener pinning effect refers to the restriction in the growth of the crystallites and grain size caused by the crystal defects like vacancies and interstitials.

Scanning electron microscopy (SEM) images of the Co-doped Al_2O_3 nanoparticles are pictured in Fig. 2a–d. Grains seem to be agglomerated for pure Al_2O_3 (Fig. 2a). Agglomeration seems to be minimized for the doped samples. A few pinholes and clustered grains are seen for the 2 wt.% Co-doped Al_2O_3 nanoparticles (Fig. 2b). Tightly packed nanosized grains were observed for the 4 wt.% Co-doped Al_2O_3 nanoparticles (Fig. 2c). With 6 wt.% Co doping, a few needle-shaped grains are observed, and agglomeration exists in a few surfaces (Fig. 2d). Thus, Co doping significantly modified the surface morphology of pure Al_2O_3.

Transmission electron microscopy (TEM) images of the Co-doped Al_2O_3 nanoparticles (Fig. 3a–d) matched exactly the results observed in the SEM images, such as agglomeration for the 0 wt.% Co-doped Al_2O_3 (Fig. 3a), clustered grains for the 2 wt.% Co-doped Al_2O_3 (Fig. 3b), tightly packed nanosized grains for the 4 wt.% Co-doped Al_2O_3 (Fig. 3c) and nanoneedles for the 6 wt.% Co-doped Al_2O_3 (Fig. 3d).

Magnetic Properties

Figure 4 shows the room-temperature magnetization versus field (M–H) loops of the Co-doped Al_2O_3 nanoparticles. It can be seen from Fig. 4a that the undoped Al_2O-$_3$exhibits paramagnetic behavior, and the samples with 2 wt.%, 4 wt.% and 6 wt.% Co doping concentrations exhibit ferromagnetic behavior with the presence of hysteresis loops (Fig. 4b–d). Thus, paramagnetic-to-ferromagnetic transition is observed in Al_2O_3 with Co doping. The origin of the ferromagnetic properties of the Al_2O_3 nanoparticles through Co doping may be attributed to: (1) intrinsic ferromagnetism, (2) secondary phases such as Co_3O_4, CoO, $CoAl_2O_4$, (3) Co clusters, (4) defects induced in the Al_2O_3 matrix due to the incorporation of Co^{2+} ions and (5) the Ruderman-Kittel–Kasuya–Yosida (RKKY) or double-exchange

Table I. $2\theta_{(0\ 0\ 2)}$, crystallite size, photoresistance, photosensitivity, degradation rate constant, saturation magnetization, retentivity and coercivity values of the Co-doped Al_2O_3 nanoparticles

Co doping concentration (wt.%)	$2\theta_{(0\ 0\ 2)}$ (°)	Crystallite size, D (nm)	Photoresistance, PR	Photosensitivity, PS	Degradation rate constant, k (min^{-1})	Saturation magnetization, M (emu/cm^3)	Retentivity (emu/cm^3)	Coercivity (Oe)
0	32.74	39	− 9.01	7.5	0.01462	–	–	–
2	32.72	37	− 7.17	11	0.0174	8.82×10^{-5}	1.13×10^{-5}	8
4	32.69	33	− 3.37	15.1	0.0245	2.05×10^{-4}	4.29×10^{-5}	18
6	32.71	35	− 4.28	13.2	0.02101	1.42×10^{-4}	3.44×10^{-5}	10

mechanism in which electrons or holes due to the substitution of Co ions induce ferromagnetism.[25] Literature results showed that dipole–dipole interaction is the main reason for the observed ferromagnetism at low temperatures.[26] It has been reported that oxygen vacancies created in nonmagnetic oxide semiconductors through doping play a dominant role in inducing magnetic moments in them by creating bound magnetic polarons (BMPs).[27] In the Al_2O_3 matrix doped with Co^{2+} ions, an electron locally trapped by an oxygen vacancy (V_o) has an important function on the spin orientations of neighboring Co ions. The magnetic exchange interactions between V_o and Co ions align some of the spin of Co ions around V_o, forming BMPs. Hence, greater densities of oxygen vacancies yield a greater volume occupied by BMPs, thereby enhancing ferromagnetism.[28] The magnetic parameters such as saturation magnetization (M_s), retentivity and coercivity values of the Co-doped Al_2O_3 nanoparticles are compiled in Table I. The realization of ferromagnetism confirmed that when Co-doped Al_2O_3 nanoparticles are used as photocatalysts for the degradation of organic dyes, they can be easily separated from the dye solution by a magnet or an applied magnetic field for taking absorption spectra and to perform reusable and stability tests.

Optical Characterization

Figure 5 shows the FTIR spectra of (a) undoped and (b) Co-doped Al_2O_3 nanoparticles. The peaks observed in the wavenumber region 3657–3137 cm^{-1} and the peak observed at around 1637 cm^{-1} for the undoped and doped samples may be attributed to OH stretching and bending vibrations, respectively.[29,30] The peaks observed at 2008 cm^{-1} for the undoped sample and at 2017 cm^{-1} for the doped samples may be attributed to N–H stretching vibration.[31] The peak at 1751 cm^{-1} may be due to deformation vibration of the adsorbed water molecules.[32] The C=O stretching vibration peak is observed at around 1405 cm^{-1} for all the samples.[33]

An Al–OH bond-related peak is observed at 1072 cm^{-1} for the undoped sample and at 1068 cm^{-1} for the doped samples.[15] Peaks related to C–N stretching vibration are observed at 1028 cm^{-1} for all the samples.[34] The peak at 982 cm^{-1} observed for the undoped sample may be attributed to C–O band.[30] An Al–O infrared vibration peak is observed at 765 cm^{-1} for the Co-doped Al_2O_3 nanoparticles.[30] Metal–oxygen (MO)-related bands are observed at 621 cm^{-1}, at 527 cm^{-1} for the undoped sample, at 618 cm^{-1} for the 4 wt.% and 6 wt.% Co-doped Al_2O_3 samples and at 532 cm^{-1} for the 4 wt.% Co-doped sample.[35]

The UV–Vis absorption spectra for pure Al_2O_3 and Co-doped Al_2O_3 nanoparticles with different concentrations of dopant Co are shown in Fig. 6. The absorbance values depend on the particle size

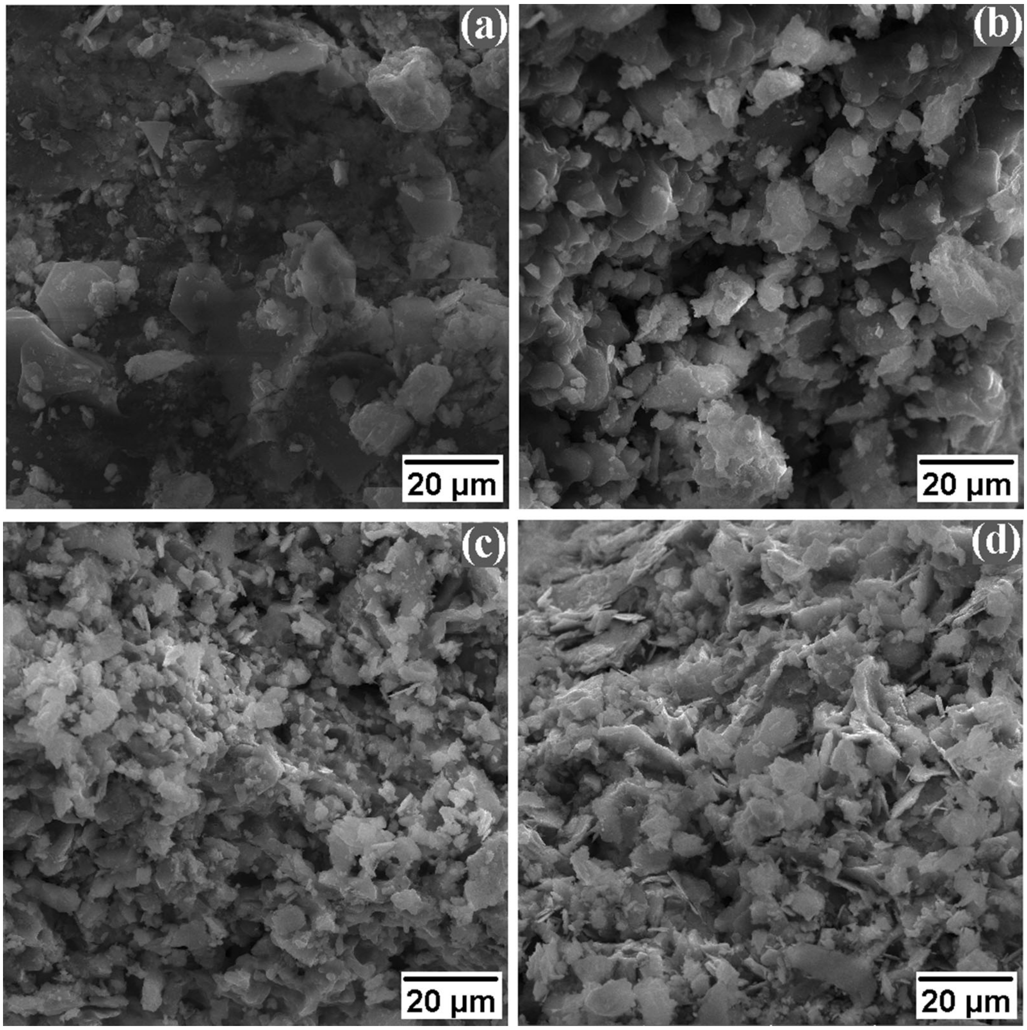

Fig. 2. SEM images of (a) 0 wt.%, (b) 2 wt.%, (c) 4 wt.% and (d) 6 wt.% Co-doped Al_2O_3 nanoparticles.

and defects in the Al_2O_3 crystal lattice. The absorbance edge values of the 0 wt.%, 2 wt.%, 4 wt.% and 6 wt.% Co-doped Al_2O_3 nanoparticles were 326 nm, 332 nm, 341 nm and 338 nm, respectively. It can be seen that the absorption edges of pure Al_2O_3 shift toward the higher-wavelength side (red shift) with Co doping, inferring a reduction in the bandgap values of the doped samples. The bandgap energy (E_g) values of the Co-doped Al_2O_3 nanoparticles were calculated using the equation[36]:

$$E_g = \frac{1240}{\lambda_{max}} \mathrm{eV} \qquad (2)$$

where λ_{max} is the absorption edge. The bandgap energies of the pure Al_2O_3 and Co-doped Al_2O_3 nanoparticles were 3.80 eV, 3.73 eV, 3.64 eV and 3.67 eV, respectively. The variation in the bandgap energy may be related to the crystal structure, phase composition, particle size and morphology of the Co-doped Al_2O_3 nanoparticles.[37] The *sp-d* exchange interaction between the band electron and the localized d electrons of the substituted dopant ions shifts the bandgap energy of pure Al_2O_3 towards lower energies.[38] Due to this, the recombination rate of the photo-induced electrons and holes decreases which improved the photocatalytic activity of the Co-doped Al_2O_3 nanoparticles (Section: Photocatalytic Properties).

Figure 7 shows the room-temperature PL spectra of the Al_2O_3 nanoparticles synthesized with 0 wt.%, 2 wt.%, 4 wt.% and 6 wt.% Co doping concentrations recorded by exciting the samples at $\lambda = 320$ nm. Emission peaks were observed for all the samples at 361 nm, 377 nm, 410 nm, 493 nm, 506 nm, 521 nm and 545 nm, respectively. The near-band-edge (NBE) UV emission peaks observed at 361 nm and 377 nm may be due to the recombination of free excitons.[39] Similar NBE emissions have been reported earlier for $Zn_{1-x}Cd_xO$ ($0 \leq x \leq 0.1$) nanopowders.[40] Direct transitions from the conduction band to the valence band caused by the interstitials might be responsible for the peak at 410 nm.[41] Rajput et al.[42] reported the occurrence of similar metal ion interstitials-related transition at 424 nm. The peak at 493 nm is due to oxygen

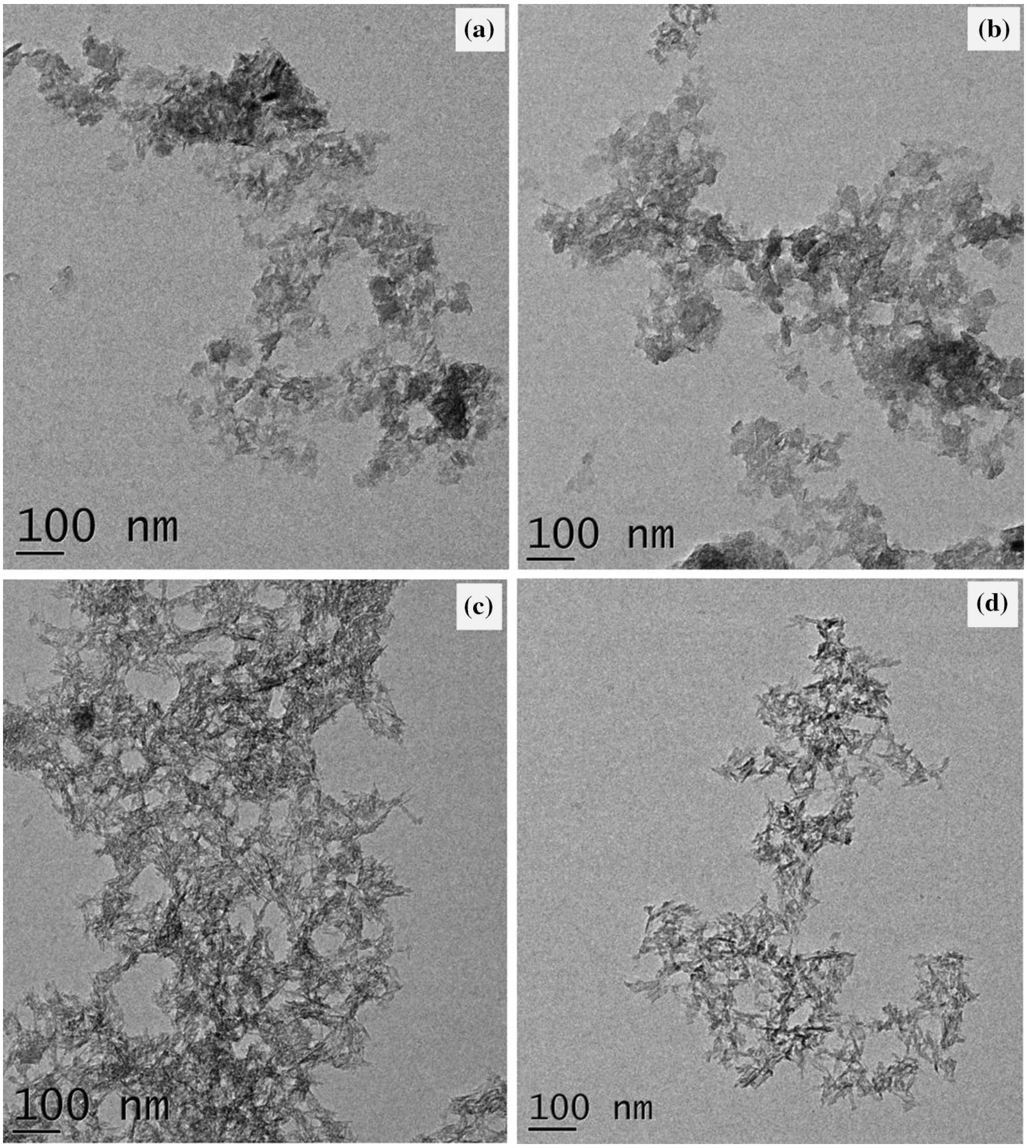

Fig. 3. TEM images of (a) 0 wt.%, (b) 2 wt.%, (c) 4 wt.% and (d) 6 wt.% Co-doped Al_2O_3 nanoparticles.

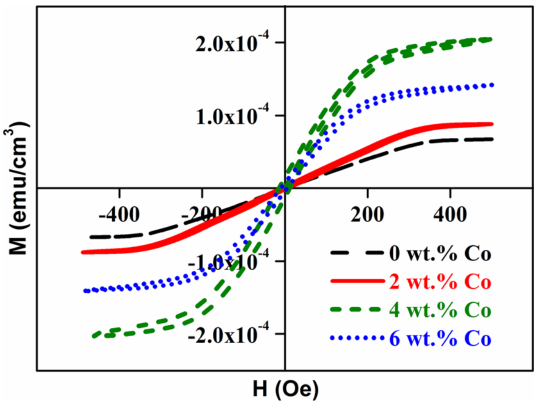

Fig. 4. M–H curves of the Co-doped Al_2O_3 nanoparticles.

vacancies present in the Co-doped Al_2O_3 nanoparticles.[2] Khodadadi et al.[43] attributed that the peak at 493 nm is a network defect induced by the excitation of the oxygen down the conduction band in the Al_2O_3 matrix. Donor–acceptor pair (DAP)-related emission is observed at 506 nm.[44] The recombination of a photogenerated hole and the electron of a singly ionized oxygen vacancy is responsible for the emission peak at 521 nm.[17] The recombination of the conduction band with the interstitial oxygen (O_i) might be responsible for the emission peak at 545 nm.[45]

Photoresistance (PR) and photosensitivity (PS) values of the Co-doped Al_2O_3 nanoparticles were calculated from the *I*–*V* characteristics of the

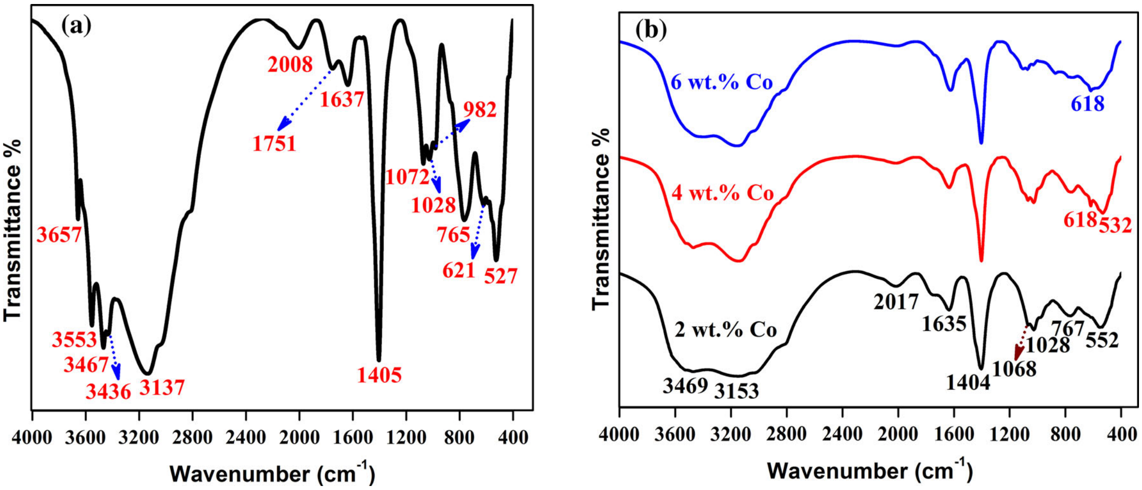

Fig. 5. FTIR spectra of (a) undoped and (b) Co-doped Al_2O_3 nanoparticles.

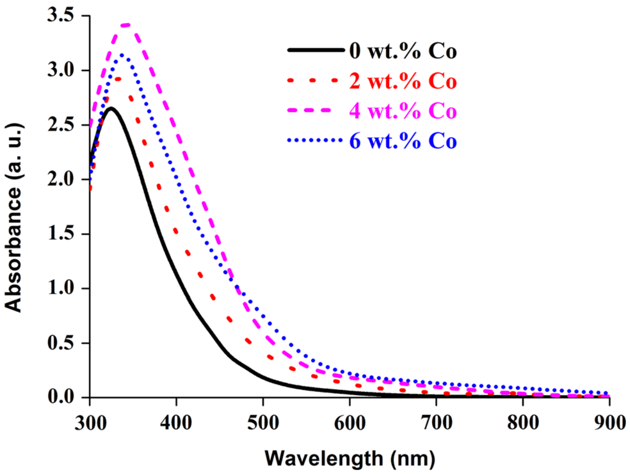

Fig. 6. Absorbance spectra of the Co-doped Al_2O_3 nanoparticles.

samples taken under dark (Fig. 8a) and light (Fig. 8b) conditions using the formulae[46]:

$$\mathrm{PR} = \frac{R_i - R_d}{R_d} \tag{3}$$

$$\mathrm{PS} = \frac{I_{\mathrm{ph}} - I_d}{I_d} \tag{4}$$

where R_d and I_d are the resistance and current values measured in dark, respectively; R_i and I_{ph} are the resistance and current values measured in light conditions. The PR and PS values are compiled in Table I. The photosensitivity values of pure Al_2O_3 increased with increase in Co doping concentration. Thus, the light-harvesting ability of pure Al_2O_3 improves with Co doping, and the Co-doped Al_2O_3 nanoparticles exhibit better photocatalytic abilities (Section: Photocatalytic Properties).

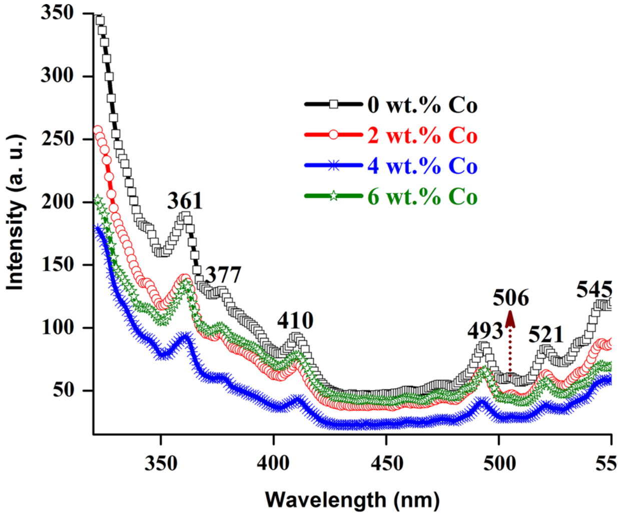

Fig. 7. PL spectra of the Co-doped Al_2O_3 nanoparticles.

Photocatalytic Properties

Rhodamine B (RhB), a cationic dye, is used as the model pollutant to study the photocatalytic activity of the Co-doped Al_2O_3 nanoparticles. The photocatalytic tests were performed under visible light irradiation. The dye solutions with and without the catalysts after stirring under dark condition were irradiated under visible light using a 100-W incandescent lamp kept at 25 cm above the testing solutions with constant stirring. With increase in light irradiation time, the color of the dye starts to fade, and after 105 min of irradiation time, the dye solution with 4 wt.% Co-doped Al_2O_3 catalyst become almost colorless, confirming its higher degradation ability compared with the other samples. It is also seen that the dye solutions with the doped Al_2O_3 catalysts degraded better than the undoped Al_2O_3 catalyst (0 wt.% Co). The order of the degradation ability of the Co-doped Al_2O_3 catalysts is

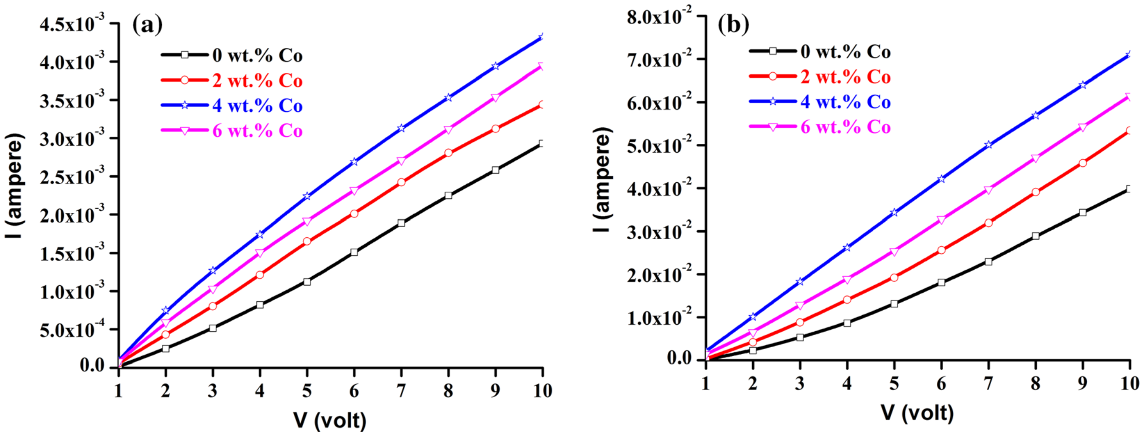

Fig. 8. *I*–*V* characteristics of the Co-doped Al_2O_3 nanoparticles recorded in (a) dark and (b) light conditions.

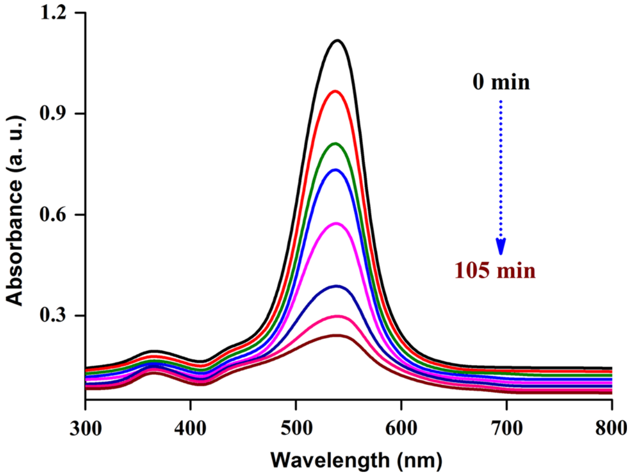

Fig. 9. Absorbance spectra of the 4 wt.% Co-doped Al_2O_3 catalyst.

4 wt.% Co > 6 wt.% Co > 2 wt.% C > 0 wt.% Co

To ascertain the degradation nature of the dye molecules, absorption spectra were recorded at $\lambda = 554$ nm, by taking 2 mL of each the tested dye solutions with 0 wt.%, 2 wt.%, 4 wt.% and 6 wt.% Co-doped Al_2O_3 catalysts at regular time intervals. The absorption peak intensities of all the samples decreased with increase in irradiation time, confirming the fact that the dye molecules degraded with light irradiation. The absorption spectra of the 4 wt.% Co-doped Al_2-O_3 catalyst is shown in Fig. 9.

From the dark (C_0) and light (C) concentrations of the dye solution, the photodegradation efficiency (η) of the Co-doped Al_2O_3 catalysts was calculated from the relation[47]:

$$\eta = \left(1 - {}^{C}\!/_{C_0}\right) \times 100 \qquad (5)$$

The degradation efficiencies of the Co-doped Al_2O_3 catalysts calculated for each irradiation time intervals are displayed in Fig. 10. Clearly, all the doped samples exhibited better degradation efficiencies than the undoped Al_2O_3 catalyst. The degradation efficiencies of the 0 wt.%, 2 wt.%, 4 wt.% and 6 wt.% Co-doped Al_2O_3 catalysts after 105 min light irradiation were found to be 78.38%, 82.35%, 95.45% and 86.44%, respectively. The degradation efficiency of 95.45% observed for the 4 wt.% Co-doped Al_2O_3 catalyst is almost comparable to the efficiency observed by Khavar et al.[48] for 7.5 wt.% Cu-doped $ZnO/Al_{\text{-}2}O_3$ photocatalyst after 60 min of sunlight irradiation, against methyl orange dye. An efficiency of 84.5% has been realized for Ag-doped Al_2O_3 catalyst by Goudarzi et al.[49] against RhB dye after 90 min of UV light irradiation. Motevalli et al.[50] reported an efficiency of 74% against methylene blue for Ag-doped AgO/Al_2O_3 nanocomposite under UV light irradiation. On comparison with the earlier reported efficiency values, the efficiency observed in this work is quite appreciable in the sense it has been achieved under

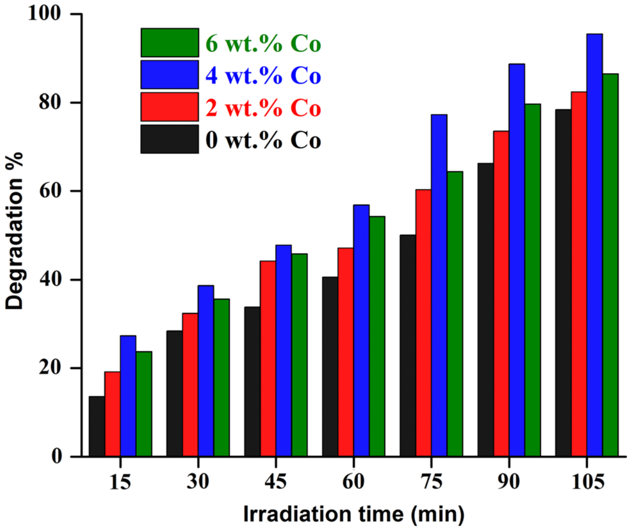

Fig. 10. Bar diagrams showing the degradation efficiencies of the Co-doped Al_2O_3 catalysts.

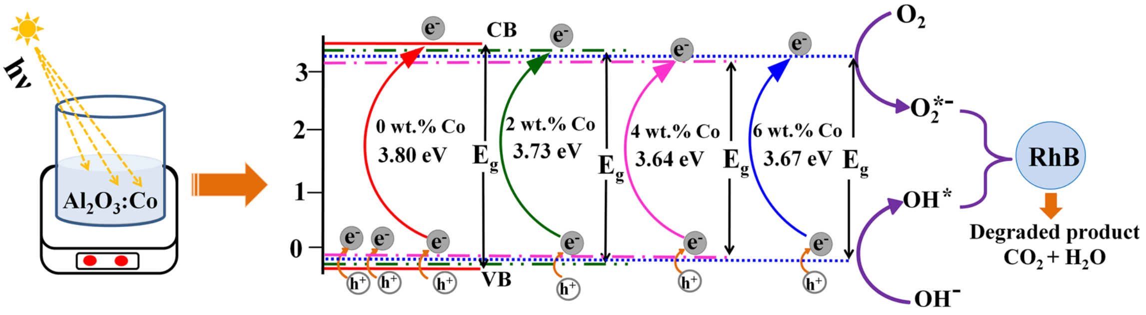

Fig. 11. Photocatalytic mechanism scheme of the Co-doped Al_2O_3 catalysts.

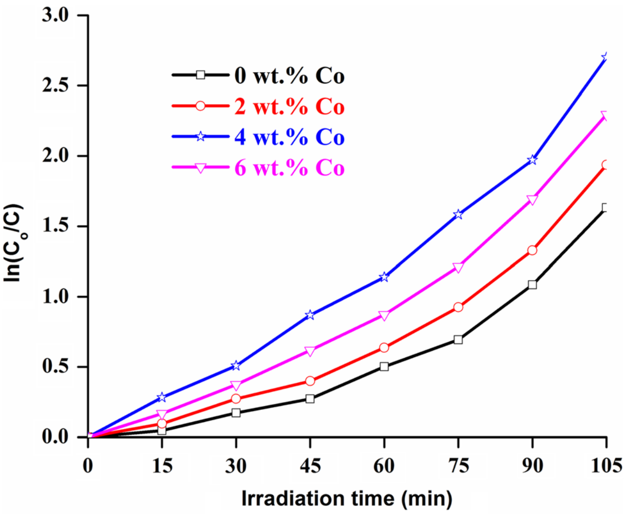

Fig. 12. Plots of $\ln\left(C_0/C\right)$ versus irradiation time of the Co-doped Al_2O_3 catalysts.

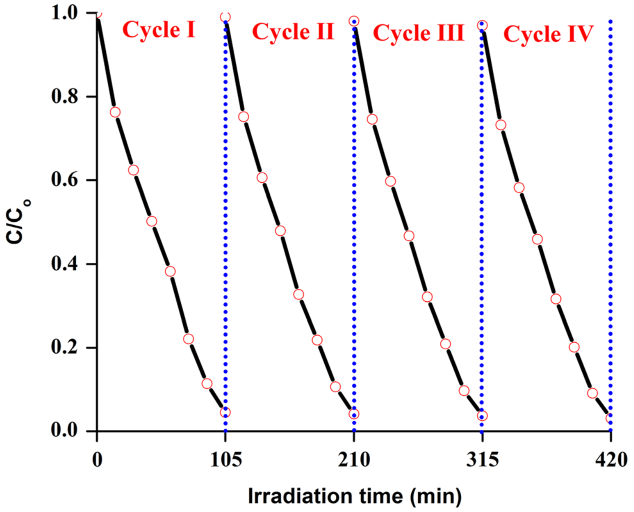

Fig. 13. Recycle tests of the 4 wt.% Co-doped Al_2O_3 catalyst.

visible light. The photocatalytic activity of the Co-doped Al_2O_3 nanoparticles rely on the generation of electron–hole (e^-/h^+) pairs on exposure to visible light. When exposed to visible light, electrons from the valence band of Al_2O_3 are excited and move to the conduction band, leaving holes in the valence band, thereby generating e^-/h^+ pairs. The electrons in the conduction band and holes in the valence band react with surrounding oxygen and water to from O_2^{*-} and OH^* radicals, which degrade the RhB dye molecules into CO_2 and H_2O,[51] as shown in Fig. 11. The increased degradation efficiency observed for the doped samples may be due to the following aspects: (1) Co in Al_2O_3 acts as a trap to capture electrons which delays the recombination of electron–hole pairs, (2) Co incorporation in Al_2O_3 creates defects in the Al_2O_3 lattice which led to an increase in the photocatalytic efficiency, (3) a decreased bandgap through Co doping might have played a role in enhancing the photocatalytic activity and (4) decreased crystallite size values through Co doping might have resulted in the creation of number of reaction sites due to increased surface area-to-volume ratio, and this facilitates the interaction between the photocatalyst and dye molecules, thereby resulting in enhanced photodegradation efficiency. Similar enhancement in the photocatalytic activity through Co doping has been reported earlier for La-Mn perovskite,[52] SnO_2,[53] ZnO[54] and ZnO/rGO nanocomposite.[20] The decreased photodegradation efficiency observed for the 6 wt.% Co-doped Al_2O_3 catalyst might be due to the active sites of Al_2O_3 being blocked due to the excess addition of dopant which produce adverse effect on the photocatalytic efficiency.[55]

The photocatalytic degradation kinetic of the Co-doped Al_2O_3 catalyst was investigated based on the pseudo first-order kinetic model proposed by Langmuir-Hinstelwood according to the equation:

$$k = \frac{\ln\left(C_0/C\right)}{t} \qquad (6)$$

where k, C_o and C are the first-order degradation rate constant, and concentrations of the dye under dark and light conditions, respectively, and t is the irradiation time. The 'k' values calculated from the slopes of the curves between $\ln\left(C_0/C\right)$ and irradiation time of the Co-doped Al_2O_3 catalyst (Fig. 12) are compiled in Table I. The higher values of k observed for the doped catalysts favors their increased degradation efficiencies.

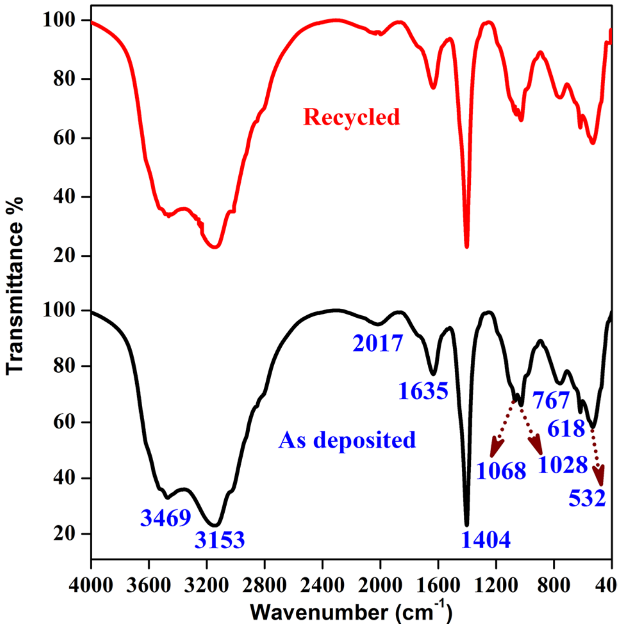

Fig. 14. FTIR spectra of as-deposited and reused 4 wt.% Co-doped Al_2O_3 catalyst.

To ascertain the stability and reusable nature of the Co-doped Al_2O_3 catalysts, recycle tests were performed for several cycles for the 4 wt.% Co-doped Al_2O_3 catalyst which exhibited the maximum degradation efficiency. Up to four cycles, no significant variation was observed in the efficiency, and after the fourth cycle, a slight loss in efficiency was observed (Fig. 13). To examine the reusable nature, FTIR spectra were taken. Figure 14 shows the FTIR spectra of as-deposited (a) and recycled (b) 4 wt.% Co-doped Al_2O_3 catalyst. Both spectra resemble the same, confirming the more stable and reusable nature of the Co-doped Al_2O_3 catalysts. Thus, the Co-doped Al_2O_3 nanoparticles are well suited for photocatalytic applications with appreciable efficiency, stability and a reusable nature.

CONCLUSION

The effect of Co doping on the structural, optical, photoconductive, photocataltyic and magnetic properties of Al_2O_3 nanoparticles synthesized via precipitation method has been reported in this paper. Decreased crystallite size and optical bandgap values have been observed for the doped samples. Photocatalytic studies confirmed that Co^{2+} ions improved significantly the degradation efficiency of pure Al_2O_3 under visible light irradiation. Among the doped catalysts, the 4 wt.% Co-doped Al_2O_3 catalyst exhibited a maximum degradation efficiency of 95.45% against RhB dye. Recycle tests confirmed the more stable nature of the Co-doped Al_2O_3 catalysts. Thus, Co-doped Al_2O_3 catalysts are well suited for practical applications with appreciable degradation efficiency. Also, due to the magnetic orderings induced in Al_2O_3 through Co doping, the Co-doped Al_2O_3 catalysts exhibited regenerable and reusable potentials.

ACKNOWLEDGMENTS

SAIF, Cochin is very much thanked for the TEM images.

REFERENCES

1. A. Umar, M.S. Akhtar, A. Al-Hajry, M.S. Al-Assiri, and N.Y. Almehbad, *Mater. Res. Bull.* 47, 2407 (2012).
2. N. Manjula, G. Selvan, and A.R. Balu, *J. Mater. Sci.: Mater. Electron.* 29, 3657 (2017).
3. K. Nagaveni, G. Sivalingam, M.S. Hegde, and G. Madras, *Appl. Catal. B. Environ* 48, 83 (2004).
4. J. Wu, H.Y. Zhang, L. Wei, X. Liu, and B. Xu, *J. Coll. Inter. Sci.* 324, 167 (2008).
5. E.S. Agorku, A.T. Kuvarega, B.B. Mamba, A.C. Pandey, and A.K. Mishra, *J. Rore Earth Met.* 33, 198 (2015).
6. L. Gao, Y. Li, Q. Li, Z. Song, and F. Ma, *Nanotechnol.* 28, 215201 (2017).
7. M. Farahmandjou and S. Motaghi, *Opt. Commun.* 441, 1 (2019).
8. Q. Yuan, A.X. Yin, C. Luo, L.D. Sun, Y.W. Zhang, W.T. Duan, H.C. Liu, and C.H. Yan, *J. Am. Chem. Soc.* 130, 3465 (2008).
9. R. Doremus, Alumina, in: J. Shackelford, R. Doremus (Eds), (Springer US, 2008), pp. 1–26.
10. M. Vahtrus, M. Umalas, B. Polyakov, L. Dorogin, R. Saar, M. Tamme, K. Saal, R. Lohmus, and S. Vlassov, *Mater. Charact.* 107, 119 (2015).
11. A. Adak, M. Bandyopadhyay, and A. Pal, *J. Environ. Sci. Health* 40, 167 (2005).
12. M.C. Patterson, N.D. Keilbart, L.W. Kiruri, C.A. Thibodeaux, S. Lomnicki, R.L. Kurtz, E.D. Poliakoft, B. Dellinger, and P.T. Springer, *Chem. Phys.* 422, 277 (2013).
13. E. Mohammadifar, F. Shemirani, B. Majidi, and M. Ezoddin, *Desal. Water. Treat.* 54, 758 (2015).
14. L. El Mir, A. Amlouk, and C. Barthou, *J. Phys. Chem. Sol.* 67, 2395 (2006).
15. S. Balamurugan, A.R. Balu, V. Narasimman, G. Selvan, K. Usharani, J. Srivind, M. Suganya, N. Manjula, C. Rajashree, and V.S. Nagarethinam, *Mater. Res. Exp.* 6, 015022 (2019).
16. H. Balard, A. Mansour, E. Papier, and P. Pichat, *J. Chem. Phys.* 82, 1051 (1985).
17. S. Anbarasu, S. Ilangovan, V.S. Nagarethinam, J. Srivind, S. Balamurugan, M. Suganya, and A.R. Balu, *Nano-Struct. Nano-Objects* 17, 67 (2019).
18. S. Ravishankar, A.R. Balu, S. Balamurugan, K. Usharani, D. Prabha, M. Suganya, J. Srivind, and V.S. Nagarethinam, *J. Mater. Sci.: Mater. Electron.* 29, 6051 (2018).
19. A. Sutka, T. Kaambre, R. Parna, I. Juhnevica, M. Maiorov, U. Joost, and V. Kisand, *Sol. State Sci.* 56, 54 (2016).
20. Y. Miao, X. Wang, W. Wang, C. Zhou, G. Feng, J. Cai, and R. Zhang, *J. Energy Chem.* 26, 549 (2017).
21. Z. Nasir, M. Shakir, R. Wahab, M. Shoeb, P. Alam, R.H. Khan, and M. Mobin, *Int. J. Biol. Macromol.* 94, 554 (2017).
22. R. Swapna and M.C. Santhosh kumar, *J. Phys. Chem. Sol.* 74, 418 (2013).
23. B.D. Culity, *Elements of x-ray diffraction*, 2nd ed. (MA: Addison Wesley, 1978), pp. 102–103.
24. S. Swanboon, P. Amorpitoksuk, and A. Suklorat, *Ceram. Int.* 37, 1359 (2011).
25. A. Goktas, I.H. Mutlu, and Y. Yamada, *Superlattices Microstruct.* 57, 139 (2013).
26. B.J. Sarkar, A. Bandyopadhyay, J. Mandal, A.K. Deb, and P.K. Chakrabarti, *J. Alloys Compnd.* 656, 339 (2016).
27. J.M.D. Coey, M. Venkatesn, and C.B. Fitzzerald, *Nat. Mater.* 2, 173 (2005).
28. N.W. Gray and A. Tiwari, *J. Appl. Phys.* 110, 033903 (2011).

29. P. Samiyammal, K. Parasuaramn, and A.R. Balu, *Superlattices Microstruct.* 129, 28 (2019).
30. J. Srivind, V.S. Nagarethinam, M. Suganya, S. Balamurugan, K. Usharani, and A.R. Balu, *Vacuum* 163, 373 (2019).
31. D. Prabha, S. Ilangovan, S. Balamurugan, M. Suganya, S. Anitha, V.S. Nagarethinam, and A.R. Balu, *Optik* 142, 301 (2017).
32. J. Srivind, V.S. Nagarethinam, S. Balamurugan, S. Anitha, M. Suganya, D. Prabha, and A.R. Balu, *Surf. Interfaces* 9, 58 (2017).
33. F. Liu, X. Shao, J. Wang, S. Yang, H. Li, X. Meng, X. Liu, and M. Wang, *J. Alloys Compnd.* 551, 327 (2013).
34. M. Mousavi-Kamazani, Z. Zarghami, and M. Salavati-Muasari, *J. Phys. Chem. C* 120, 2096 (2016).
35. K. Laishram, R. Mann, and N. Malhan, *Ceram. Int.* 38, 1703 (2012).
36. S. Anitha, M. Suganya, D. Prabha, J. Srivind, S. Balamurugan, and A.R. Balu, *Mater. Chem. Phy.* 211, 88 (2018).
37. B. Roya, S. Chakrabartyaq, O. Mondala, M. Palb, and A. Duttaa, *Mater. Charact.* 70, 1 (2011).
38. C. Aydin, M.S. Abd El-sadek, K. Zheng, I.S. Yahia., and F. Yakuphanoglu, Opt. Laser Technol. 48, 447 (2013).
39. N. Manjula and A.R. Balu, *Optik* 130, 464 (2017).
40. Y.R. Sui, Y. Cao, X.F. Li, Y.G. Yue, B. Yao, X.Y. Li, J.H. Lang, and J.H. Yang, *Ceram. Int.* 41, 587 (2015).
41. D. Antosoly, S. Ilangovan, V.S. Nagarethinam, and A.R. Balu, *Surf. Eng.* 34, 682 (2018).
42. J.K. Rajput, T.K. Pathak, V. Kumar, M. Kumar, and L.P. Purohit, *Surf. Interfaces* 6, 11 (2017).
43. A. Khodadadi, M. Farahmandjou, M. Yaghoubi., and A.R. Amani, 16, 718 (2019).
44. N. Manjula, M. Suganya, D. Prabha, S. Balamurugan, J. Srivind, V.S. Nagarethinam, and A.R. Balu, *J. Mater. Sci.: Mater. Electron.* 28, 7615 (2017).
45. M. Suganya, A.R. Balu, D. Prabha, S. Anitha, S. Balamurugan, and J. Srivind, *J. Mater. Sci.: Mater. Electron.* 29, 1065 (2018).
46. R. Nallendran, G. Selvan, and A.R. Balu, *J. Mater. Sci.: Mater. Electron.* 29, 11384 (2018).
47. D. Prabha, K. Usharani, S. Ilangovan, M. Suganya, S. Balamurugan, J. Srivind, V.S. Nagarethinam, and A.R. Balu, *Mater. Technol.* 33, 333 (2018).
48. A.H. Cheshme Khavar, A. Mahjoub, and M. Bayat Rizi, *J. Photochem. Photobio. B* 175, 37 (2017).
49. M. Goudarzi, Z. Zarghami, and M.S. Niasari, *J. Mater. Sci.: Mater. Electron.* 27, 9789 (2016).
50. K. Motevalli, M. Ebadi, and Z. Salehi, *J. Mater. Sci.: Mater. Electron.* 28, 13024 (2017).
51. M. Suganya, S. Anitha, D. Prabha, S. Balamurugan, J. Srivind, and A.R. Balu, *Mater. Technol.* 33, 214 (2018).
52. M. Dhinam, M. Tripathi, and S. Singhal, *Mater. Chem. Phys.* 202, 40 (2017).
53. L.M. Fang, X.T. Zu, Z.J. Li, S. Zhu, C.M. Liu, and L.M. Wang, *J. Mater. Electron.* 19, 868 (2008).
54. M.G. Nair, M. Nirmala, K. Rekha, and A. Anukaliani, *Mater. Lett.* 65, 1797 (2011).
55. M. Huang, C. Xu, Z. Wu, Y. Huang, J. Lin, and J. Wu, *Dyes Pigment* 77, 327 (2008).